Ph.D. Thesis Dissertation

Experimental estimation of soil emissivity and its application to soil moisture retrieval in the SMOS mission

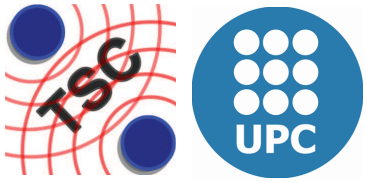

Alessandra Monerris i Belda

Remote Sensing Laboratory
Dept. Teoria del Senyal i Comunicacions
Universitat Politècnica de Catalunya

Ph.D. Thesis advisors

Dr. Adriano J. Camps Carmona & Dr. Mercè Vall-llossera Ferran

Barcelona, June 2009

A Fina, Julián i Òscar,
pel seu suport incondicional.

A Adriano i Mercè,
per donar-me l'oportunitat de dur a terme aquesta tesi.

Acknowledgements

The author would like to thank the following institutions which have contributed, in one way or another, to this work:

- Spanish Ministry of Science and Education grant FPU AP2003-1567, hold by the author from 2004 to 2007.
- Spanish Ministry of Science and Education projects MIDAS-2 ESP2002-11648-E, MIDAS-3 ESP2004-00671, and MIDAS-4 ESP2005-06823-C05-02, for funding the field experiments reported in this PhD Thesis.
- The Land Use Planning department from the Centro de Investigaciones sobre Desertificación (CIDE) and the Thermodynamics and Climatology from Satellites group from the University of Valencia for their participation in the SMOS REFLEX campaigns.
- The Joint Research Center (JRC) from the European Commision for providing the MOUSE 2004 experiment site facilities.
- The Universitat de Lleida and the Institut de Recerca i Tecnologia Agroalimentàries for their participation in the T-REX experiments.

Summary

Although water hold by soils represents a small fraction of the Earth's water budget, soil moisture plays an important role in climate models. In the near future, two space missions will measure soil moisture at global scale: ESA' SMOS and NASA's SMAP. The present Ph.D. Thesis has been performed in the context of the SMOS (Soil Moisture and Ocean Salinity) mission pre-launch activities over land. An important feature of SMOS is that a given pixel on the Earth is imaged at various observation angles as the satellite moves over it, so multi-angular information of each pixel will be available.

A description of the field campaigns over land carried out by the Universitat Politècnica de Catalunya and of their results is provided in this PhD Thesis. Radiometric measurements were acquired using the UPC L-band Automatic Radiometer (LAURA), which has a working frequency of 1.4 GHz, the same as SMOS payload MIRAS. The execution of these experiments, the data processing, and the physical interpretation of measurements constitute the core of this PhD Thesis. The emissivity of land surfaces depends upon the interaction of several soil and vegetation characteristics such as soil moisture, roughness, and temperature, and vegetation opacity and albedo. Each of the experiments focused on one of the parameters affecting the emission from soils:

- MOUSE 2004: impact of soil texture on soil moisture and temperature profiles, soil emissivity, and the impact on the soil moisture retrieval using multi-angular dual-polarisation radiometric observations.
- T-REX 2004/2006: impact of soil roughness on the brightness temperature. Data are compared to simulations using various models for the effective soil roughness.
- SMOS REFLEX 2003/2006: effects of rock-fraction and vines. The brightness temperature dependence on soil moisture and observation position is studied, and soil moisture retrieval is discussed.
- TuRTLE 2006: impact of topography on soil emissivity at L-band.

Results suggest that the SMOS Level 2 soil moisture processor should select the soil dielectric constant model as a function of soil texture, since the root mean squared error can vary from 2% to 7% depending. Soil roughness was found to have a strong impact on land brightness temperature, especially for dry soils. In general, all semi-empirical land emission models follow the trend of dry soils measurements at H-pol, whereas discrepancies exist for wet soils. On the other hand, vines opacity and albedo were found to be independent on the polarisation. The error between ground-truth and estimated soil moisture over vineyards was 2.3%, better than the 4% required for SMOS. Topography effects are important and cannot be accounted for in the models only by the introduction of the vegetation canopy.

Contents

Chapter 1

Introduction

This chapter justifies the importance of measuring soil moisture at global scale, and describes the motivation of and context in which this work has been developed. The state-of-the-art of ground-based and space-borne projects involving passive microwave sensors and dealing with soil water content measurements is shortly described. Special interest is payed to the European Space Agency Soil Moisture and Ocean Salinity (SMOS) mission, since this Ph.D. Thesis has been performed as part of the preparatory activities for this mission.

1.1 Motivation

About 70% of the Earth is covered with water, 97% of which is part of oceans. Heating of oceans by the Sun keeps the Earth's water in a continuous circulation from the atmosphere to the Earth and back to the atmosphere through condensation, evapotranspiration, and precipitation processes. Figure 1.1 illustrates this continuous water motion which is called the water or hydrologic cycle. Some of the precipitation that falls onto the land infiltrates into the ground and becomes groundwater. The groundwater in the unsaturated or vadose zone of land is usually referred to as soil moisture. The thickness of this zone extends from soil surface to a few metres below the surface in humid regions, and to 300 m or more below surface in arid regions. Although the water hold by soils is a small fraction of the Earth's water budget, soil moisture plays an important role in the water cycle since controls the proportion of rainfall that percolates, runs off, or evaporates from the land, influences plants growth and transpiration, and is related to the precipitation variability within a region [Koster *et al.*, 2004].

A better understanding and modelling of the Earth climate implies a good knowledge of the global water cycle [Entekhabi *et al.*, 1999, Krajewski *et al.*, 2006]. Although soil moisture is one of the main parameters used in climate models, in-situ measurements of soil moisture are sparse and their values are only representative of small areas, since soil moisture temporal and spatial variation is large. Present climate models estimate soil moisture using general circulation models such as the data base in Robock *et al.* [2000]. Remote sensing with sufficient accuracy would provide meaningful soil moisture data over large regions. The operating frequency of

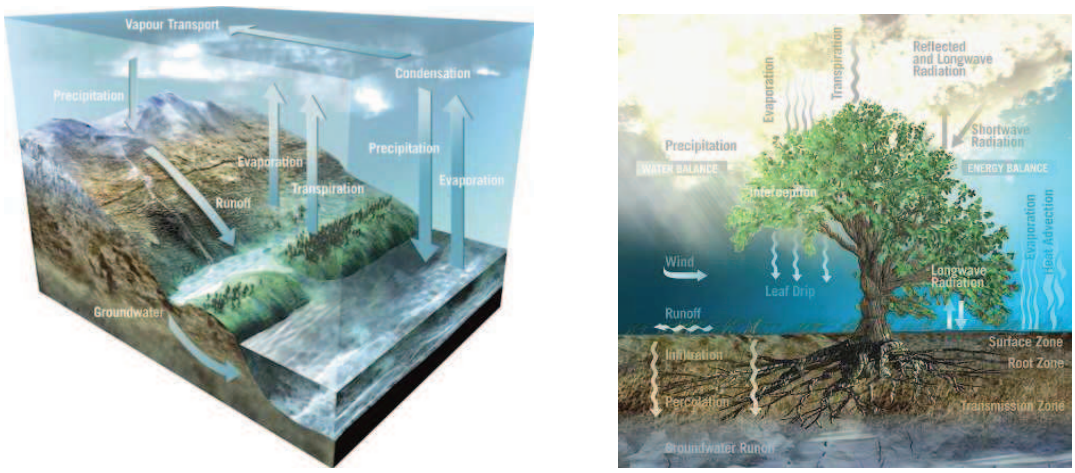

Fig. 1.1: Earth's water cycle (credits: ESA)

the remote sensing system must be chosen so that its sensitivity to water is maximum. Figure 1.2 represents the brightness temperature sensitivity to soil moisture, soil roughness, vegetation biomass, and atmospheric parameters as a function of frequency. The maximum sensitivity to soil moisture is achieved in the lower range of microwave frequencies, which goes from 1 to 5 GHz (wavelength from 30 cm to 5 cm, respectively). The justification to this behaviour can be found if the dielectric properties of a target are analysed, since they have a large influence on its microwave brightness temperature. Land surfaces can be considered as a mixture of soil, water, and air particles and thus soil moisture might be estimated from measurements if the contrast between the water and soil particles were large enough. This contrast is achieved at microwave frequencies, at which the real part of dry soil and water dielectric constants are approximately 4 and 80, respectively [Jackson & Schmugge, 1989]. Many works in the scientific literature conclude that microwave radiometry at L-band (1.4–1.427 GHz) is optimal to estimate soil moisture, not only because it is very sensitive to soil moisture, but also because provides all-weather coverage, since the atmosphere at microwave frequencies may be considered nearly transparent, and vegetation is semi-transparent, which allows observations of the underlying layers [Eagleman & Lin, 1976, Wang & Choudhury, 1981, Jackson & Schmugge, 1991, 1995, Kerr *et al.*, 2000].

1.2 Satellite missions for soil moisture estimation

L-band microwave sensors provide maximum sensitivity to soil moisture. However, achieving an adequate ground resolution, which would be in the order of 50 km or less, using classical solutions on low-orbit satellites implies an antenna size of up to 20 m. At present, different scientific groups are developing new techniques to face this problem, and two space missions have been proposed to measure soil moisture at global scale: ESA' SMOS and NASA's SMAP.

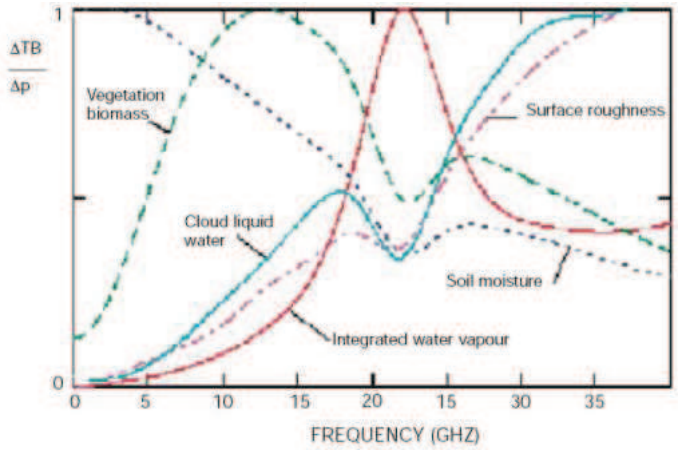

Fig. 1.2: Brightness temperature sensitivity to soil moisture, soil roughness, vegetation biomass, and atmospheric parameters as a function of frequency (credits: ESA)

1.2.1 The Soil Moisture and Ocean Salinity mission

The Soil Moisture and Ocean Salinity (SMOS) mission will observe soil moisture over land and salinity over oceans, and will measure snow and ice areas contributing to studies of the cryosphere [ESA, 2003, Kerr *et al.*, 2001, Barré *et al.*, 2008]. Scheduled for launch in autumn 2009, it is the second Earth Explorer mission and part of the European Space Agency's Living Planet Programme.

SMOS was thought of as a cost-effective, demonstrator mission with a nominal (extended) lifetime of 3 (5) years. The orbit is quasi-circular, sun-synchronous and dawn-dusk, and will be in the low-Earth range, at 763 km. The SMOS mission is a completely new approach in the field of remote sensing at L-band (1.4–1.427 GHz) by employing a novel instrument called MIRAS (Microwave Radiometer by Aperture Synthesis) developed by EADS-CASA Espacio (Madrid, Spain). The payload is mounted on a generic Proteus platform developed by the French Space Agency (CNES), and will be put in orbit by a Russian Rockot launch vehicle. The total launch mass is 683 kg, comprising 366 kg for payload and 317 kg for platform.

To satisfy the scientific requirements, SMOS aims at providing global maps of soil moisture every 3 days with a ground resolution better than 50 km, and 0.04 m^3/m^3 volumetric humidity. This soil moisture accuracy is referred pixels outside mountainous, urban, and partially frozen or snow-covered areas. For sea salinity, maps with an accuracy better than 1.2 psu and 200 km ground resolution, will be acquired every 30 days. SMOS mission requirements are summarised in Table 1.1. The satellite will be operated from CNES' control centre near Toulouse, France, using ESA's Kiruna tracking station, while data will be downloaded to a processing centre at ESA's European Space Astronomy Centre (ESAC) at Villafranca del Castillo, Spain.

The Microwave Imaging Radiometer by Aperture Synthesis

SMOS payload, MIRAS, is an aperture synthesis radiometer which measures brightness temperature at 1.413 GHz. This novel instrument is the first-ever two-dimensional interferometric radiometer in space and will provide much-needed data for climate models. MIRAS consists

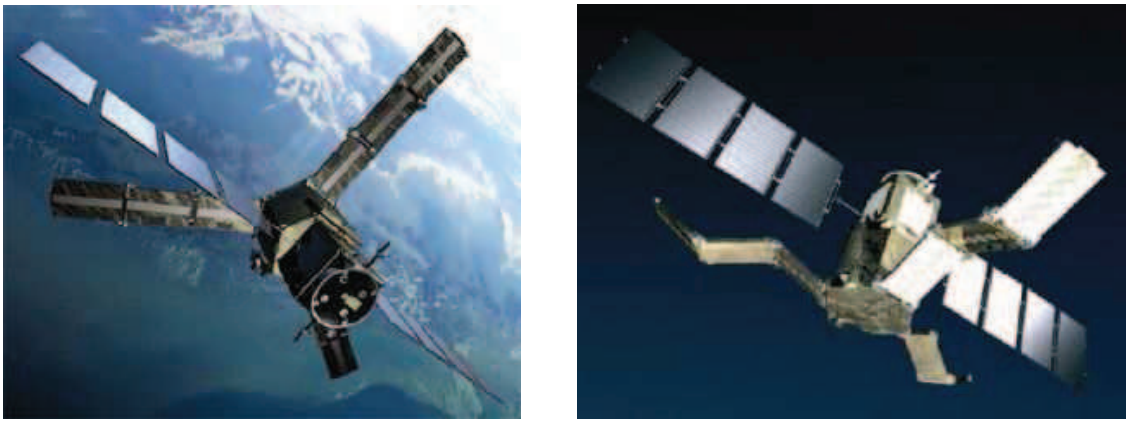

(a) (b)

Fig. 1.3: Artist's view of (a) SMOS-MIRAS, and (b) in-orbit deployment of SMOS (from www.esa.int)

Table 1.1: SMOS mission requirements

Global coverage	80° North/South latitude
Spatial resolution	50 km
Revisit time	3 days
Swath width	1050 km to 640 km
SM accuracy	4%
OS accuracy	1.2 psu
Nominal (extended) lifetime	3 (5) years
Geo-localisation accuracy	400 m

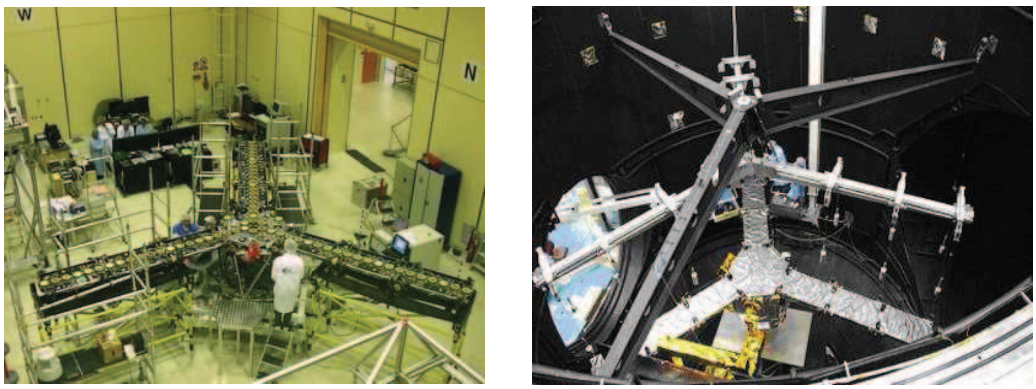

(a) (b)

Fig. 1.4: (a) MIRAS instrument at EADS-CASA facilities (from www.esa.int). (b) MIRAS during the Image Validation Test campaign at ESA-ESTEC Maxwell anechoic chamber premises in spring 2007 (courtesy of EADS-CASA Espacio)

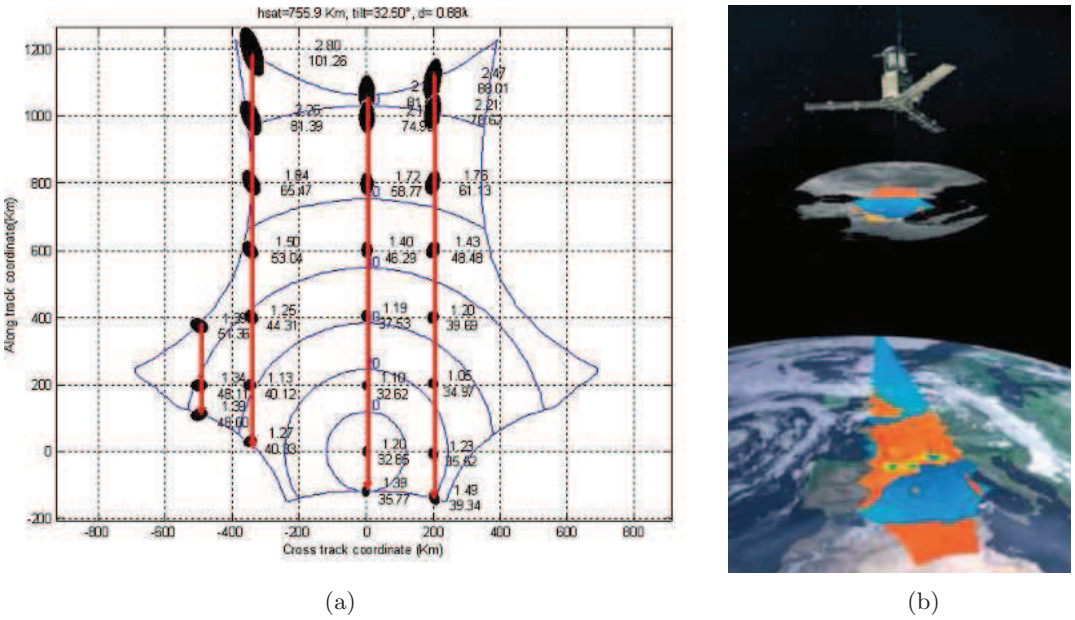

(a) (b)

Fig. 1.5: (a) Hexagonal SMOS field of view. Blue lines indicate the observation angle, black ellipses indicate the pixel size depending on the position within the snap-shot, and red lines show how a single pixel can be observed under different viewing positions during a satellite overpass. (b) MIRAS brightness temperature images in the antenna coordinates and lat/long coordinates (from www.esa.int).

of a Y-shaped antenna array with three arms, each arm having an approximate length of 4.5 m and 21 dual-polarisation L-band antennæ or LICEF (Light Cost Effective Front-end) spaced 0.875λ. Each LICEF is a total power radiometer in its own. Nine redundant antennæ and three full-polarimetric noise injection radiometers are located in a fixed structure in the centre of the array, while the arms are divided in three segments to be folded during the launch as shown in Fig. 1.3(b). On board calibration is performed by injecting a known noise signal into all the LICEF many times per orbit. An external absolute calibration will be performed every two weeks with celestial targets [McMullan *et al.*, 2008].

MIRAS has two operation modes: dual polarisation or full-polarimetric. In the dual polarisation mode brightness temperatures are measured at H- and V-pol alternately using an integration time of 1.2 s, while in the full-polarimetric mode the third and fourth Stokes' parameters are also acquired [Martín-Neira *et al.*, 2002]. The radiation acquired by each antenna is transmitted to a central correlator unit which performs the complex cross-correlation between every pair of receivers. The data is stored on-board and transmitted using an X-band down-link whenever a ground station is seen by SMOS. The prime contractor for MIRAS is EADS-CASA Espacio, Spain, while the LICEFs have been developed by Mier Comunicaciones, Spain. Pictures of MIRAS taken at EADS-CASA and ESA-ESTEC facilities are shown in Fig. 1.4.

If classical solutions would have been used, with this antenna size and orbit altitude the field of view (FOV) would be of near 3000 km in diameter. However, because of the microwave interferometry technique, the instrument Y-shape, and the antennæ spacing, the resulting FOV is an hexagonal-like area of less than 1000 km, as shown in Fig. 1.5. The spatial resolution varies from 35 km at the FOV centre to 50 km at the border. Over land, the radiometric sensitivity

for a 1.2 s integration time varies from 3.5 to 5.8 K while, in the case of oceans, the expected radiometric sensitivity is to be within 2.5 and 4.1 K. MIRAS will provide observations of a single azimuth at various incidence angles (from 0° to 55° , blue circles in Fig. 1.5) and radiometric resolutions depending on its position within the field of view during a satellite overpass. This fact will much improve the retrieval algorithms because a lot of independent information of each pixel is registered, and will permit the estimation of soil roughness, vegetation opacity and albedo, etc. jointly with soil moisture.

MIRAS airbone demonstrators

AMIRAS, which stands for Airborne MIRAS (also known as SMOSillo), is a small version of the SMOS payload designed as a demonstrator of the two-dimensional radiometry technique. AMIRAS consists of a Y-shaped array with four second generation LICEFs per arm and it is able to measure in both dual- and full-polarimetric modes. The first outdoor campaign was carried in April 2006 at the Institut de Recerca i Tecnologia Agroalimentarias (IRTA), near the delta of river Ebro, Spain, with the aim of testing several calibration schemes. Images of the Milky Way and the Sun and two flights over land and ocean were successfully carried out with AMIRAS [Duffo *et al.*, 2007]. For further information refer to Martín-Neira *et al.* [2008].

The Helsinki University of Technology (HUT) has also developed a MIRAS demonstrator named HUT-2D, which has 36 receivers distributed in a U-shaped array along three arms. HUT-2D flew on Skyvan in April 2006, some time before AMIRAS, and succesfully acquired a galaxy image.

SMOS mission products

The SMOS mission products will be divided into four categories:

- Level 0 products: unprocessed SMOS data with added Earth Explorer headers. Level 0 products include, for instance, satellite data, and calibration data from correlators.
- Level 1 products are divided into three subcategories:
  1. *Level 1a* products are calibrated visibilities grouped as snapshots.
  2. *Level 1b* products are vectors of brightness temperatures referred to the antenna polarisation reference frame and grouped as snapshots.
  3. *Level 1c* products are brightness temperatures referred to a fixed grid on a Earth ellipsoid and sorted into swath-based maps. Level 1c products are generated separately for land and sea applications.
- Level 2 products are soil moisture or surface salinity swath-based maps which have been computed from Level 1c products. The conversion from Level 1c brightness temperatures to Level 2 maps includes a first step to mitigate the impact of Faraday rotation, Sun/Moon/galactic glint, atmospheric attenuation, etc. and is done separately for soil moisture and ocean salinity.

- Level 3 products are based upon the spatio-temporal resampling of Level 2 products.

- Level 4 products are improved Level 2/3 products through the use of auxiliary data from other sources.

Level 0 to Level 2 data products will be archived for 10 years after the end of the SMOS extended operational lifetime (EEOL) in orbit. Further information on these levels is given in Zundo *et al.* [2005].

1.2.2 SMAP mission

The Hydrosphere State (HYDROS) mission was proposed by NASA to enhance the understanding of the land hydrosphere state and improve the climate prediction models [Entekhabi *et al.*, 2004, Njoku *et al.*, 2004]. The mission had a circular, polar, sun-synchronous, 6 am/pm equator crossing orbit located at 670 km altitude. Hydros aimed at providing soil moisture estimates with a 4% volumetric accuracy in the top 2–5 cm, and capturing freeze/thaw state transitions in integrated vegetation-soil continuum at the spatial scale of landscape variability (3 km). The payload consisted of both active and passive sensors. An L-band (1.41 GHz) radiometer measured the first, second, and third Stokes parameters with a 40 km spatial resolution, and 1 K relative accuracy. On the other hand, an L-band (1.26 GHz) radar acquired VV, HH, and HV polarisations with a 10 km resolution and 0.5 dB accuracy for VV and HH. Observations at a constant incidence angle between 35° and 50° . Both the radar and the radiometer share a 6 m diameter reflector antenna which rotates about its nadir axis.

NASA stopped funding HYDROS in 2005, but many HYDROS science and technology issues are being reviewed to be implemented in the future Soil Moisture Active and Passive (SMAP) mission [NASA, 2007].

1.3 Soil moisture field experiments

Space missions for Earth observation require a huge amount of previous work to validate the existing science and technology. This is accomplished through airborne or ground-based field experiments. Table 1.2 provides a list of the radiometers available for SMOS cal/val activities. On the other hand, Table 1.3 summarises some of the campaigns that have been conducted in the last years over land surfaces using L-band radiometers. Most of these radiometers have been designed within the context of preparatory activities previous to a space mission launch. Some of the radiometers existing at present are listed in Section 1.3.1. Next sections shortly explain the forementioned experiments, classified into two groups depending on their link to the SMOS mission.

1.3.1 L-band ground-based radiometers

EMIRAD

The dual-polarisation L-band (1.41 GHz) radiometer EMIRAD was built at the Technical University of Denmark (TUD). Its antenna is square shaped horn with a base of 61 × 61 cm approximately, a height of 85 cm, and a -3 dB beamwidth of 25° . It has an 8 s integration time and gives brightness temperature measurements every second with 1 K accuracy and 0.1 K sensitivity [Søbjærg, 2002]. Second generation EMIRAD radiometers have been built to be used during SMOS Cal/Val.

ELBARA

ELBARA was constructed in 2001 at the University of Bern, Switzerland. It is a dual-polarisation Dicke radiometer with an internal two-point calibration. ELBARA is equipped with a conical horn antenna (diameter 1.4 m, length 2.7 m) and has a −3 dB beamwidth of 12° and 1 K accuracy. A picture of this instrument can be found in Fig. 1.6(a) and more information in [Mätzler *et al.*, 2003].

LEWIS

LEWIS (L-band radiometer for Estimating Water In Soils) is a L-band dual-polarisation radiometer by CNES-CESBIO-ONERA, France. LEWIS is equipped with a 1.3 m diameter Potter horn antenna working at 1.4 GHz. The −3 dB beamwidth is 13.6° , the beam efficiency is greater than 98%, and has almost no rear lobes. The instrument resolution is 0.2 K for a 4 s integration time, and the estimated accuracy is 0.5 K [Lemaître *et al.*, 2004]. A picture of LEWIS is shown in Fig. 1.6(e).

LAURA

LAURA (L-band AUtomatic RAdiometer) is a fully-polarimetric Dicke radiometer working at a frequency of 1.4135 GHz. LAURA has been used since 2000 by the UPC in multiple field campaigns both over sea and land, such as those presented in this thesis. Further information is given in Section 4.1 and in Villarino [2004].

ESTAR

ESTAR (Electronically Scanned Thinned Array Radiometer) was jointly developed by the Goddard Space Flight Center, the University of Massachusetts, and the USDA Agricultural Research Service. The objective was to demonstrate the 1D aperture synthesis concept for Earth observations. ESTAR is an H-polarisation hybrid of a real and a synthetic aperture radiometer. The along track resolution is obtained by means of real antenna aperture, while the across track resolution is obtained synthetically. Different soil moisture experiments at the USDA research watersheds in Arizona and Oklahoma were a success. Unfortunately, the proposed space mission

based on the ESTAR concept, HYDROSTAR, was not selected by NASA for the Earth System Science Pathfinder in 1998. More information on ESTAR can be found in LeVine *et al.* [1994].

STARRS

STARSS (Salinity, Temperature, and Roughness Remote Scanner) is a push broom radiometer 8 × 8 microstrip patch array which measures six cross track beams simultaneously at V-polarisation and builds a 2D image as it moves along track.

PALS

PALS (Passive/Active L/S band radiometer) was designed by the Jet Propulsion Laboratory to measure ocean salinity and soil moisture. The instrument has both a radar and a dual-frequency (L- and S- band), dual-polarisation radiometer. The L-band antenna has diameter of 1 m and a length of 2.7 m. The instrument bandwidth at L-band is 20 MHz, the beam efficiency is 92%, the cross polarisation isolation 20 dB, and the absolute accuracy is <2 K [Wilson *et al.*, 2001].

RaDomeX

RaDomeX was designed at the Institute for Applied Physics (IFAC) to study the long term stability of the microwave emission in Antarctica and the possibility of using this area as SMOS external calibration target. The radiometer has a dual polarisation Potter antenna working at 1413 MHz. The instrument bandwidth is 27 MHz, the expected sensitivity 0.2 K, the expected accuracy <1 K , and the −3 dB beamwidth is 20° [Macelloni *et al.*, 2007].

ISU-L

ISU-L is an L-band, dual-polarisation, total power radiometer from the Iowa State University. Its antenna is a Potter horn with a 3 dB beamwidth for horizontal (vertical) polarisations of 20.3° (18.4°) in elevation and 17.9° (20.4°) in azimuth, respectively. The highest sidelobe level is 26.8 dB down from boresight, return losses are better than -17 dB, and NEΔT is 0.3 K over a 10 s integration period [De Roo *et al.*, 2006]. A picture of this radiometer is shown in Fig. 1.6(f).

PAU-RAD

The L-band Passive Advanced Unit Radiometer (PAU-RAD) is, jointly with the GPS-reflectometer (PAU-GNSS/R) and the infra-red radiometer (PAU-IR), part of the PAU project from the UPC to retrieve the sea surface salinity. PAU-RAD is a digital, full polarimetric radiometer with a 4×4 array antenna whose elements are separated 0.63 wavelengths at the GPS L1 frequency (1.57542 GHz). To avoid the mechanical scan, the beamforming is digital. The beam can be steered up to 20° from the array boresight (45° incidence angle) in 5° steps, which means that the incidence angle ranges from 25° to 65° [Camps *et al.*, 2007, Bosch-Lluís *et al.*, 2007].

ComRAD

The Combined Radar/Radiometer (ComRAD) system was developed jointly by NASA/GSFC and the George Washington University (GWU) to verify the applicability of active and passive instruments in a combined manner for predicting the microwave emission from soils. A 1.22 m parabolic dish reflector is shared by both the radiometer (1.4 GHz) and radar (1.25 GHz) instruments by using a single broadband stacked-patch dual-polarised feed [O'Neill *et al.*, 2006]. ComRAD will be used in a three years project, which started in the summer of 2006, to acquire data at tree sites cover a wider range of seasonal and soil moisture conditions [O'Neill *et al.*, 2007].

1.3.2 Field experiments in the frame of SMOS mission

Most of the field experiments carried out during the last years as part of the SMOS preparatory activities over land are summarised in Table 1.3. Those performed by the UPC and which have provided the data for this Ph.D. Thesis are presented in Chapter 4. The others, are briefly described in the following sections.

EuroSTARSS

EuroSTARRS is an airbone experiment conducted in November 2001 over six different sites in France and Spain in coordination with many scientific groups [Berger *et al.*, 2002]. The objectives were multiple, as were the observed scenarios: characterising the relationship of vegetation opacity and look angle, estimating multi-angular emission from different land covers and soil moisture conditions, studying topography effects, mixed-pixel retrieval validation, retrieval sensitivity to pixel size variation, urban areas emission, sea salinity retrieval validation and azimuthal effects investigation. Data were acquired by the US L-band radiometer STARSS. The instrument was mounted on a Dornier 228 plane by DLR and acquired multi-angular observations up to 50° . Gravimetric and TDR soil moisture measurements, air and surface physical temperature and vegetation characterisation, salinity.

Table 1.2: L-band ground-based radiometers available for SMOS cal/val

Name	Owner	Polarisations	3 dB beamwidth	Aperture	Beams
ComRAD	NASA/GWU	dual	12.5°	real	1
ELBARA 1, 2, 3	ESA	dual	12°	real	1
EMIRAD	TUD	full	23° or 31°	real	1
IROE	IFAC	dual	35°	real	1
ISU-L	ISU	dual	19°	real	1
LAURA	UPC	full	20°	real	1
LEWIS	CESBIO	dual	13.6°	real	1
PAU-RAD	UPC	dual/full	20°	real,dig. beamforming	multiple
RaDomeX	IFAC	dual	35°	real	1

Table 1.3: Summary of L-band field campaigns over land performed in the last fifteen years. Acronyms stand for USA (United States of America), UK (United Kingdom), FR (France), SP (Spain), NL (The Netherlands), CH (Switzerland), GE (Germany), IT (Italy), and AU (Australia).

Date	Campaign	Site	Surface	Instrument
1992/1994	Washita	Oklahoma (USA)	agricultural	ESTAR,AIRSAR,PBMR
1997/1999	SGP97/99	Oklahoma (USA)	agricultural	ESTAR, PSR, PALS
1999	ESSC	Reading (UK)	bare	SWaMP-L
2001	INRA	Avignon (FR)	bare, corn	EMIRAD
2001	EuroSTARRS	Toulouse (FR), Utiel (SP)	many	STARSS
2002	ETH	Eschikon (CH)	bare	ELBARA
2002	SMEX	Iowa (USA)	various	ESTAR, PSR, PALS, AIRSAR
2003/2006	SMOS REFLEX	Utiel (SP)	vines	LAURA
2003	ELBARA 2003	Wageningen (NL)	bare, grass	ELBARA
2003-2006	SMOSREX	Toulouse (FR)	bare, fallow	LEWIS
2003	SMEX	OK, AL, GA (USA)	various	2DSTAR, PSR, AIRSAR
2004	SMEX	Arizona, Mexico (USA)	various	2DSTAR, PSR
2004	MOUSE	Ispra (IT)	bare	LAURA
2004/2006	T-REX	Agramunt (SP)	bare	LAURA
2004	ETH	Eschikon (CH)	grass	ELBARA
2004	Bray	Les Landes (FR)	forest	EMIRAD
2005	ETH	Julich (GE)	forest	ELBARA
2005	SMEX	Iowa (USA)	various	APMIR
2005	NAFE	Upper Hunter (AU)	grassland, forest	EMIRAD, PLMR
2006	TuRTLE	El Brull (SP)	mountain	LAURA
2006/2007	MELBEX I/II	Utiel (SP)	shrub/vines	EMIRAD
2006	NAFE	Yanco (AU)	various	PLMR
2007	CLASIC	Oklahoma (USA)	various	PSR, PALS
2008/2009	GRAJO	Vadillo (SP)	grass,barley,bare	LAURA, GPS-Interferometer

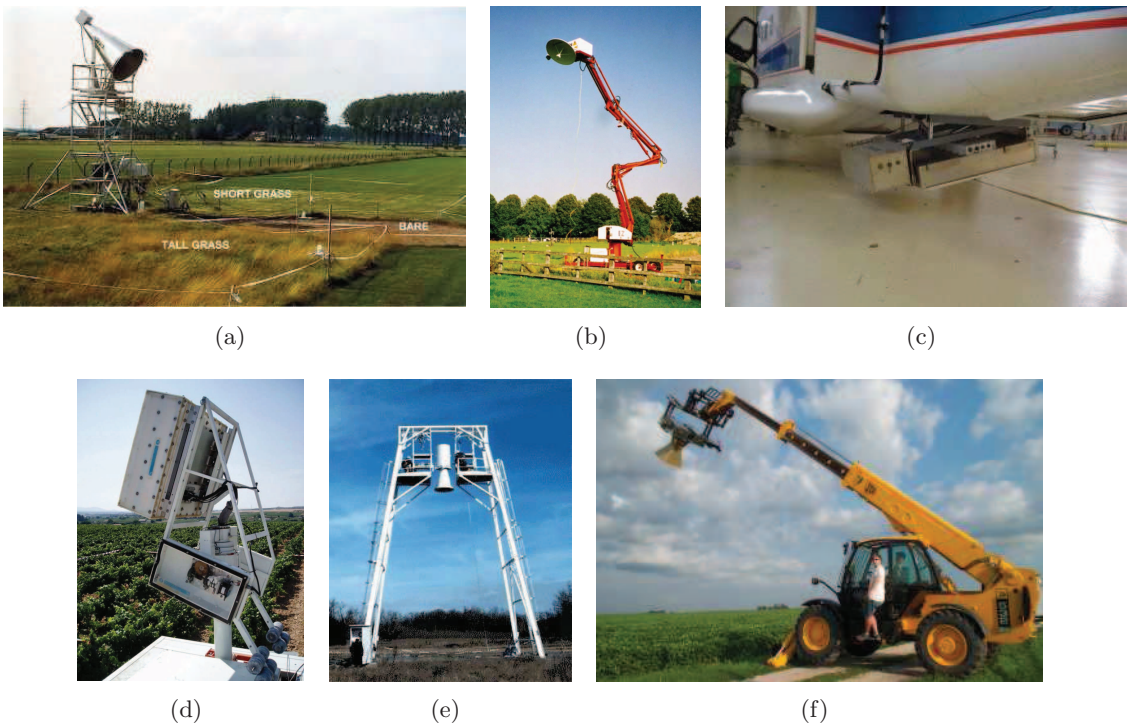

Fig. 1.6: L-band radiometers which have been employed in field experiments over land. (a) ELBARA (credits: VUA), (b) SWaMP-L, (c) STARRS (credits: ESA), (d) LAURA, (e) LEWIS (credits: CESBIO), (f) ISU-L (credits: Iowa State University)

ELBARA 2003

The experiment was conducted by the Vrije Universiteit Amsterdam from April to September 2003 at Wageningen (The Netherlands, 51° 58′ N and 5° 38′ E, altitude 7 m). The experimental site consisted of three different areas as shown in Fig. 1.6(a): one bare site, a grassland mowed at a regular basis (15 cm average), and a grassland kept undisturbed (from 15 cm in April up to 50 cm in July). Radiometric data were continuously measured at an incidence angle of 52.5° with the L-band radiometer ELBARA, which was mounted on top of a 5 m scaffolding tower jointly with other three infrared radiometers. Soil moisture and temperature measurements were acquired in all the three sites at 0, 2, 5, 7.5, and 15 cm depth using TDR sensors and soil thermistors. First results show that brightness temperature at vertical polarisation is less sensitive to water storage in the vegetation canopy, and that measurements are sensible to dew and changes in the vegetation biomass [De Jeu *et al.*, 2004].

SMOSREX

The Surface Monitoring Of the Soil Reservoir EXperiment (SMOSREX) is a long-term field campaign conducted by INRA since January 2003. The experimental site is located in Toulouse, France (43° 23′ N, 1° 17′ E, 188 m altitude) and consists of two plots, one of them bare and the other covered by fallow. The LEWIS radiometer is installed 15 m above the ground, and measures the brightness temperature at incidence angle between 20° and 60° every 10° . Mete-

orology, heat fluxes, soil moisture and temperature profiles, soil texture, and biomass are also measured.

A high correlation between the polarisation ratio and the bare soil moisture during a 19 months period was obtained. In contrast, a direct correlation between soil moisture and polarisation ratio was not found in the fallow site. An increase in the vegetation emission after a rainfall event was observed. This fact shows that the water content variations of litter affect the microwave emission [de Rosnay *et al.*, 2006]. The impact of soil roughness on each polarisation and its angular dependence has also been analysed. A different influence of roughness on V- and H-polarisation was found, as well as an increase with incidence angle at V-pol and a decrease at H-pol [Escorihuela *et al.*, 2007].

Bray 2004

The Bray field campaign was carried out at Les Landes production forest, France (44° 42′ N, 0° 46′ W, altitude 61 m) by INRA. The area mainly consists of Maritime Pines with an approximate height of 22 m, distributed in a grid with an inter-row spacing of 4 m. On top of the soil was a litter layer whose thickness exceeded 10 cm. The EMIRAD radiometer was mounted on a 40 m tower with a look direction 20° from North. Measurements were done automatically at 25° to 60° incidence angle from nadir, every 5° . Surface temperature was measured using a thermal IR radiometer mounted next to EMIRAD. Concurrently with the radiometric measurements, soil temperature was measured at four different locations at eight different depths using thermocouples. Litter temperature was recorded at 1, 3 and 5 cm above the mineral soil surface. Moreover, soil and litter moisture content were measured using ThetaProbes [Grant *et al.*, 2007]. In February 2006 and February 2007 additional fieldwork was done to measure separately the radiometric properties of canopy, grass understory, litter and soil.

CoSMOS

The ESA sponsored airborne Campaign for validating the operation of SMOS (CoSMOS) was designed to perform long-term acquisitions under different geo/bio-physical, meteorological, and oceanographic conditions to address open issues related to the retrieval and validation of the SMOS products. Initially scheduled for Spring 2005, CoSMOS was cancelled.

However, the soil moisture campaign was finally carried out from 31 October to 25 November 2005 in the frame of the National Australian Field Experiment (NAFE) [Merlin *et al.*, 2008, Saleh *et al.*, 2007b]. The test site located 200 km west of Newcastle, Australia, had been used to soil moisture studies for some time now so there were permanent monitoring stations which provided meteorological data and soil moisture profiles. Different European institutions (Free University of Amsterdam, University of Valencia, Technical University of Denmark, and CESBIO) and the University of Melbourne were involved. The radiometric measurements were taken from an aircraft carrying a polarimetric L-band radiometer developed specifically for coSMOS by the TUD. The radiometer has two large antenna horns so the ground was viewed from two different angles simultaneously.

On the other hand, the sea salinity campaign CoSMOS-OS was conducted during four weeks in April 2006 across the Norwegian Coast. Twelve flights, eight at night and four Sun-glint flights in the morning, were performed. The scientific payload consisted of the EMIRAD radiometer from the TUD, Denmark, and an infrared profiler and the GOLD-RTR reflections instrument from IEEC-CSIC, Spain. In-situ measurements were provided by NIVA and oil drilling platforms.

MELBEX

The Modelling of L-Band emission of natural vegetation Mediterranean species EXperiment (MELBEX) was a joint initiative of the UVEG (Spain), INRA (France), and TUD (Denmark). From May 2005 to February 2006 radiometric measurements over natural shrubs were acquired using the EMIRAD radiometer [Cano *et al.*, 2007]. The experiment was repeated in 2007 over vines at the Valencia Anchor Station, Utiel, Spain [Cano *et al.*, 2008].

1.3.3 Other field experiments

Southern Great Plains experiments

The Southern Great Plains (SGP) experiments were conducted by NASA and USDA in Oklahoma, USA, in 1997 and then again in 1999 [USDA-ARS, 1997]. The objective was to determine if the retrieval algorithms for surface soil moisture developed at higher resolution using ground-based and airborne sensors can be extended to satellite platforms. The S- (2.65 GHz) and L-band (1.4 GHz) Microwave Radiometer (SLMR), a C band radiometer from the University of Massachusetts, and a portable thermal infrared radiometer were deployed at a boom truck at 12 m height. Measurements were acquired continuously over winter wheat and grazed pasture. Ground-based measurements were compared to airborne measurements acquired by ESTAR.

Soil Moisture EXperiments

From 2002 to 2008, NOAA, USDA, and NASA have jointly performed a series of airbone campaigns over land called Soil Moisture Experiments (SMEX) [Bindlish *et al.*, 2006, 2008]. The goal was to collect ground-based samples of soil moisture in conjunction with aircraft flights and AMSR-E (Advanced Microwave Scanning Radiometer E) overpasses and, thus, validating the soil moisture retrieval algorithm. AMSR-E radiometer was launched onboard NASA Aqua satellite and measures the microwave emission at C- and X-bands.

1.4 Objectives and organisation of the thesis

Estimation of soil moisture from radiometric measurements is not simple since the there are many soil and vegetation parameters affecting the land emission. The development of algorithms to compute bio/geophysical variables from brightness temperature measurements and the assessment of the impact of each of the parameters involved is crucial for having accurate

soil moisture estimations. This Ph.D. Thesis focuses on empirical land emission modelling and soil moisture retrieval, and it is organised as follows:

Chapter 1 describes the motivation and context in which this work has been developed. An overview of the field experiments over land carried out during the last years and of the space-borne missions involving L-band radiometers and dealing with soil water content measurements are presented.

Chapter 2 reviews the basics of microwave radiometry, and presents the types of radiometers existing nowadays.

Chapter 3 presents the existing soil emissivity and dielectric constant models, and describes the main physical properties of soils.

Chapter 4 describes the field experiments whose data have been used in this work and in which the author has actively participated, both in the campaign preparation and the analysis of the data. The ground-truth and radiometric measurements, and the experiment sites and setup are described, paying special attention to the radiometer LAURA (L-band AUtomatic RAdiometer).

Chapter 5 discusses the results from the MOUSE 2004. The impact of soil texture on soil moisture and temperature profile, soil emissivity, and soil moisture retrieval is studied.

Chapter 6 studies the impact of soil roughness on the brightness temperature. Data collected during the T-REX experiments are compared to theoretical simulations using various modelling for the effective soil roughness.

Chapter 7 analyses the data collected during the SMOS REFLEX 2003/2006, devoted to the radiometric characterisation of vineyards. The brightness temperature dependence on soil moisture and observation angle is studied, and the soil moisture retrieval is discussed. The experiment site has already been selected as a SMOS calibration and validation site. This chapter also assesses the effects of rock-fraction on the soil and vineyards emission using data from the SMOS REFLEX 2006 field campaign.

Chapter 8 deals with the impact of topography on soil emissivity at L-band. Data collected during the TuRTLE 2006 experiment are compared to the antenna brightness temperatures obtained by simulation of the experiment site using a facet model which considers the high resolution digital elevation model and land cover map of the area.

Chapter 9 Recent studies have shown that vegetation litter, dew, and rain interception should not be neglected in the land emission models. Although these issues have not been studied during this Ph.D. Thesis, the state-of-the art is presented for completeness of this work. Moreover, measurements of Sun and Sun glint acquired at the T-REX site are presented and discussed.

Chapter 10 Conclusions are presented, and future research lines exposed.

Chapter 2

Basics of microwave radiometry

The Earth continuously receives electromagnetic radiation coming from the Sun. Part of it is scattered and/or absorbed by the atmosphere, and the other part is transmitted to the Earth's surface. As for the latter, part is absorbed and part is scattered outwards. The energy absorbed by a body is transformed into thermal energy, which translates into an increase of its temperature until the thermodynamic equilibrium is reached. Then, according to Thermodynamics, the body radiates energy to keep the energy balance. Radiometry is the field of science which studies the thermal electromagnetic energy radiated by the bodies. Radiometers are instruments capable of measuring the power emitted by a body with high resolution and accuracy. The basic concepts of microwave radiometry are reviewed in this chapter.

2.1 Brightness and power collected by an antenna

The power emitted by a source in a solid angle and by unit surface is called brightness $B(\theta, \phi)$ [W·sr^{-1}m^{-2}],

$$B(\theta, \phi) = \frac{F_t(\theta, \phi)}{A_t}, \tag{2.1}$$

and depends on a directional distribution function $F_t(\theta, \phi)$ and the total radiating area A_t.

The power collected by an antenna which is surrounded by an incident power $B(\theta, \phi)$ is [Ulaby *et al.*, 1986]

$$P = F_t \cdot \frac{A_r}{R^2} = B \cdot A_t \cdot \frac{A_r}{R^2}, \tag{2.2}$$

where A_r is the effective area of the antenna and R is the distance between the antenna and the radiating target. If the solid angle of the transmitting antenna Ω_t is defined as

$$\Omega_t = \frac{A_t}{R^2}, \tag{2.3}$$

then (2.2) can be expressed as follows

$$P = B \cdot A_r \cdot \Omega_t. \tag{2.4}$$

In the general case represented in Fig. 2.1, where the incident brightness comes from an extended source, the power received by the antenna is

$$dP = A_r \cdot B(\theta, \phi) \cdot |F_n(\theta, \phi)|^2, \tag{2.5}$$

where $F_n(\theta, \phi)$ is the normalised antenna pattern. Moreover, if the brightness is not constant with frequency the spectral brightness density $B_f(\theta, \phi)$ is defined. Taking all these into account, the total power collected by the antenna is computed as the integration over the system bandwidth and over the space of (2.5)

$$P = \frac{1}{2} A_r \int_f^{f+\Delta f} \iint_{4\pi} B_f(\theta, \phi) |F_n(\theta, \phi)|^2 d\Omega df, \tag{2.6}$$

where Δf is the bandwidth of the receiver. Note the $1/2$ term, which indicates that only half of the randomly polarised thermal emission can be collected by the receiver antenna.

2.2 Thermal microwave radiation

All bodies at a non zero absolute physical temperature radiate electromagnetic energy due to the collision between their particles. The increase of radiated energy is proportional to the increase in temperature. The principles of thermal radiation at microwave frequencies are reviewed in this section.

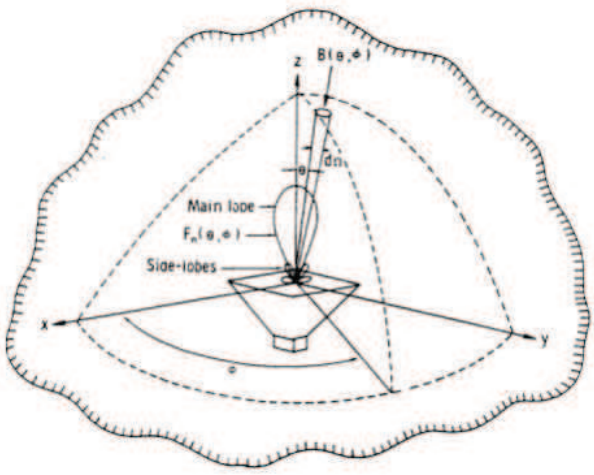

Fig. 2.1: Geometry of the incident radiation over an antenna, from [Ulaby *et al.*, 1986, p. 189]

2.2.1 Black-bodies radiation: The Plank's law

A black-body is an idealised body that absorbs all the incident radiation. Black-bodies are also perfect emitters, since otherwise their temperature would indefinitely increase. So, when thermodynamic equilibrium is reach, black-bodies radiate all the energy omnidirectionally. The spectral brightness of black-bodies is given by the Planck's law

$$B_f = \frac{2hf^3}{c^2}\left(\frac{1}{e^{hf/kT}-1}\right), \tag{2.7}$$

where f is the frequency in Hz, $h = 6.63{\cdot}10^{-34}$ Js is the constant of Planck, $k = 1.38{\cdot}10^{-23}$ J/K is the constant of Boltzmann, T is the absolute physical temperature in K, and $c = 3{\cdot}10^{8}$ m/s is the speed of light. A graphical representation of the spectral brightness density as a function of frequency for different temperatures is shown in Fig. 2.2.

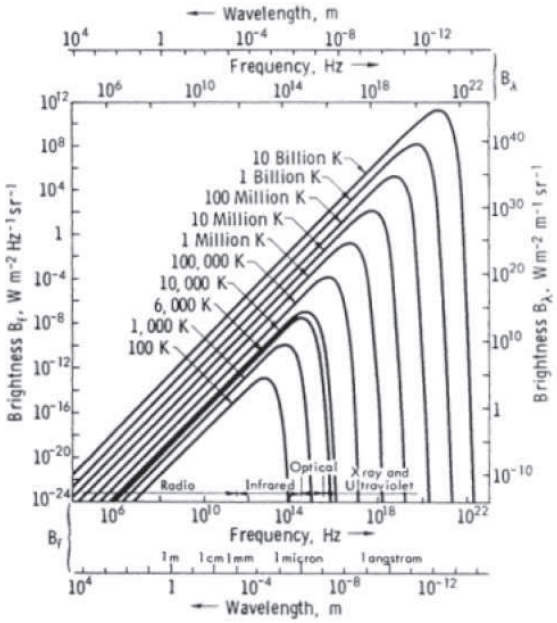

Fig. 2.2: Planck's radiation law [Ulaby *et al.*, 1986, p. 193]

At microwave frequencies $hf/kT \ll 1$ so applying the Taylor's approximation

$$e^x - 1 = \left(1 + x + \frac{x^2}{2} + ...\right) - 1 \simeq x, \qquad \text{for } x \ll 1 \tag{2.8}$$

to the exponential in (2.7), the Planck's law can be approximated by the Rayleigh-Jeans law

$$B_f \simeq \frac{2f^2kT}{c^2} = \frac{2kT}{\lambda^2}, \tag{2.9}$$

with an error smaller than 1% if f <117 GHz and T=300 K. Then, the brightness of a black

body B_{bb} at a physical temperature T and a bandwidth Δf is

$$B_{bb} = B_f \Delta_f = \frac{2kT}{\lambda^2} \Delta f. \tag{2.10}$$

It is important to note that there is a linear relationship between brightness and physical temperature at low microwave frequencies.

2.2.2 Relationship between power and temperature

The power collected by an antenna with normalised radiation pattern $F_n(\theta, \phi)$ surrounded by a black body at a constant physical temperature T_0 is given by (2.6) and (2.9)

$$P_{bb} = \frac{A_r}{2} \int_f^{f+\Delta f} \iint_{4\pi} \frac{2kT_0}{\lambda^2} |F_n(\theta, \phi)|^2 d\Omega df. \tag{2.11}$$

Assuming that the system bandwidth Δf small enough so that the spectral brightness density can be considered constant over the frequency range, then (2.11) reduces to

$$P_{\text{bb}} = \frac{kT_0 \Delta f A_r}{\lambda^2} \iint_{4\pi} |F_n(\theta, \phi)|^2 d\Omega = kT_0 \Delta f, \tag{2.12}$$

where the antenna solid angle has been expressed as a function of its effective area

$$\Omega_p = \iint_{4\pi} |F_n(\theta, \phi)|^2 d\Omega = \frac{\lambda^2}{A_r}. \tag{2.13}$$

2.2.3 Grey bodies radiation

Brightness temperature and emissivity

Contrary to black-bodies, real materials or grey-bodies do not absorb all the incident power and thus their emission is lower. The brightness of a grey body $B(\theta, \phi)$, which may depend on direction, can be described similarly to (2.10) as

$$B(\theta, \phi) = \frac{2k}{\lambda^2} T_B(\theta, \phi) \Delta f, \tag{2.14}$$

where $T_B(\theta, \phi)$ is the brightness temperature or radiometric equivalent temperature of a black body having the same brightness density. The brightness of grey-bodies relative to that of black bodies a the same physical temperature is the emissivity $e(\theta, \phi)$,

$$e(\theta, \phi) = \frac{B(\theta, \phi)}{B_{bb}} = \frac{T_B(\theta, \phi)}{T}. \tag{2.15}$$

Since $B(\theta, \phi) \leq B_{bb}$, then the emissivity is a dimensionless, polarisation-dependent parameter ranging from 1 (for perfect absorbers or black-bodies) to zero (for lossless metals which are perfect reflectors). Moreover, the brightness temperature is smaller than or equal to the physical temperature.

Apparent temperature

The apparent temperature T_{AP} is an equivalent temperature related to the total brightness incident over the antenna $B_i(\theta, \phi)$,

$$B_i(\theta, \phi) = \frac{2k}{\lambda^2} T_{AP}(\theta, \phi) \Delta f. \tag{2.16}$$

The main contribution to T_{AP} is the brightness temperature of the observed pixel T_B. However, there are other emissions that may enter the antenna lobe such as the atmospheric upward radiation T_{UP}, the radiation scattered by the land surface T_{SC}, and the atmospheric downward radiation reflected by the surface T_{DN}. So,

$$T_{AP} = T_{UP} + (T_B + T_{SC}) \frac{1}{L_a}, \tag{2.17}$$

being L_a the attenuation of the atmosphere. When measuring the Earth's brightness temperature from space it is necessary to work at frequencies that give low atmospheric attenuation. The relationship between the different contributions to T_{AP} is schematised in Fig. 2.3. According to Fig. 2.3(b), the antenna temperature T_A is estimated from the normalised antenna pattern $F_n(\theta, \phi)$ and normalised solid angle pattern Ω_p as follows

$$T_A = \frac{1}{\Omega_p} \iint_{4\pi} T_{AP}(\theta, \phi) F_n(\theta, \phi) d\Omega. \tag{2.18}$$

2.2.4 Measuring brightness temperature from space: perturbations

Many external sources may affect the brightness temperature measurements from space. At L-band, the main error sources are the Faraday rotation and the space radiation, since the contribution from the atmosphere is much smaller.

Faraday rotation

The plane of polarisation of the electromagnetic waves propagating from the Earth to the satellite through the ionosphere is rotated an angle φ. This phenomena is known as Faraday rotation and depends on the ionospheric electron content, the frequency, and the position of the ray with respect to the Earth's geomagnetic field. The lower the frequency the higher the rotation, whose daytime average is [Skou, 1989]

$$\varphi \simeq \frac{17^\circ}{f^2}, \tag{2.19}$$

where f is the frequency in GHz. The Faraday rotation mixes the polarisations as follows

$$\begin{aligned} T_{Bh}^{\text{Faraday}} &= T_{Bh} \cos^2 \varphi + T_{Bv} \sin^2 \varphi, \\ T_{Bv}^{\text{Faraday}} &= T_{Bh} \sin^2 \varphi + T_{Bv} \cos^2 \varphi. \end{aligned} \tag{2.20}$$

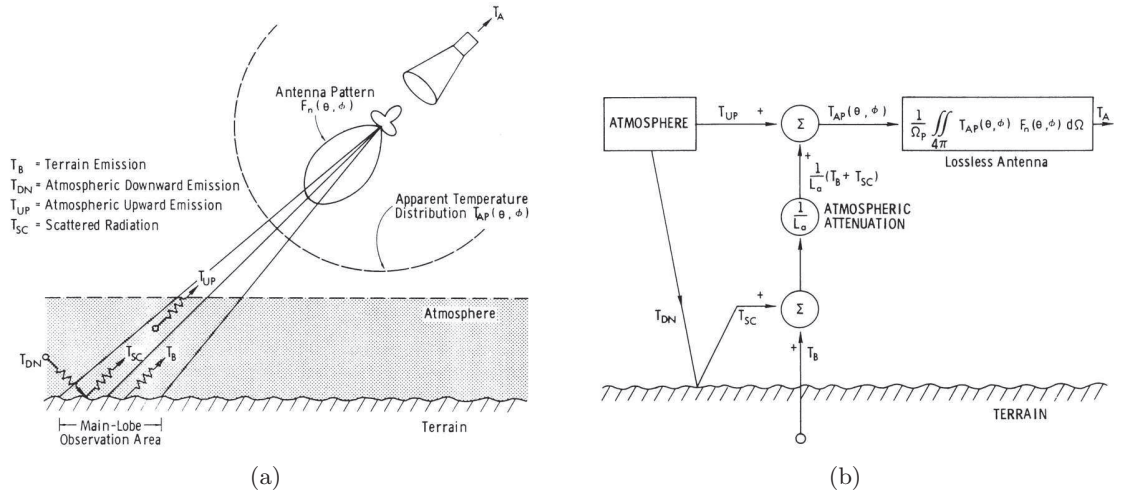

Fig. 2.3: (a) Schematic and (b) block diagram relationship between the antenna temperature T_A, the apparent temperature T_{AP}, and the brightness temperature T_B [Ulaby *et al.*, 1986, p. 202]

In the protected L-band at which SMOS operates, the mean rotation angle is 8.7° . This may result in errors on the brightness temperature of 2 K, specially critical for sea salinity estimates. Should the first Stokes parameter (see Section 2.2.5) be used in the algorithms, would measurements be independent of Faraday rotation. However, this would decrease the number of independent acquisitions in 50% and its use is still being analysed.

Space radiation

As seen in section 2.2.3 microwave radiation from space reflects over the Earth's surface and is also measured by the antenna. Three main space phenomenæ have to be considered. The first one is the cosmic radiation level, which is fairly constant (≈ 2.7 K) and thus does not affect the quality of measurements. The second phenomena is the galactic noise which varies from 0.8 K to 40 K at L-band. The noise comes from the reflection over the Earth's surface of the pole or the centre of the galaxy so a convenient orbit must be selected. If it can not be avoided it may at least be corrected using the existing maps of galactic noise. Finally, the third and most important noise source is Sun glint. The Sun brightness temperature value is higher than 10^5 K so any reflection of Sun radiation collected by the antenna would seriously affect measurement. Hence, direct reflections should be avoided by choosing a morning Sun-synchronous orbit.

2.2.5 The Stokes parameters

Plane waves can be decomposed in two orthogonally polarised components

$$E(z,t) = E_h(z,t)\vec{h} + E_v(z,t)\vec{v}, \tag{2.21}$$

which correspond to horizontal E_h and vertical E_v polarisations and are defined as

$$E_h(t) = \Re\{E_{0h}(t)e^{-j\omega t}\} = E_{0h}(t)\cos(\omega t + \delta_h)$$
$$E_v(t) = \Re\{E_{0v}(t)e^{-j\omega t}\} = E_{0v}(t)\cos(\omega t + \delta_v), \tag{2.22}$$

being $E_{0h}(t)$ and $E_{0v}(t)$ the instantaneous amplitudes of the electric field at H- and V-polarisation respectively, ω the instantaneous wave frequency, and δ_h and δ_v the phase factors.

The four Stokes parameters describe the polarisation and total energy transported by a wave, and are defined as follows:

$$\begin{pmatrix} I \\ Q \\ U \\ V \end{pmatrix} = \begin{pmatrix} T_v + T_h \\ T_v - T_h \\ T_{45^\circ} - T_{-45^\circ} \\ T_{LHC} - T_{RHC} \end{pmatrix} = \frac{\lambda^2}{kB\eta} \begin{pmatrix} \langle|E_h|^2\rangle + \langle|E_v|^2\rangle \\ \langle|E_h|^2\rangle - \langle|E_v|^2\rangle \\ 2\Re\langle E_v E_h^*\rangle \\ 2\Im\langle E_v E_h^*\rangle \end{pmatrix}, \tag{2.23}$$

where λ is the wavelength of the radiometer, k is the Boltzmann constant, B the bandwidth, and η the impedance of the medium.

The first Stokes parameter, I is the total power of the wave, while the second one, Q, is the difference between the power transported by H- and V-polarisations and represents the linear polarisation oriented in the reference direction. On the other hand, the third and fourth Stokes parameters, U and V, are the difference between the linear polarisation components oriented in 45° and −45° , and the difference between left-hand and right hand circularly polarised brightness temperature, respectively.

Polarimetric radiometers usually measure the so called modified Stokes vector, acquiring separately the energy received at H- and V-polarisations. In terms of brightness temperatures,

$$\vec{T_B} = \begin{pmatrix} T_{Bh} \\ T_{Bv} \\ U \\ V \end{pmatrix} = \frac{\lambda^2}{kB\eta} \begin{pmatrix} \langle|E_h|^2\rangle \\ \langle|E_v|^2\rangle \\ 2\Re\langle E_v E_h^*\rangle \\ 2\Im\langle E_v E_h^*\rangle \end{pmatrix}. \tag{2.24}$$

The Dicke radiometer LAURA (L-band AUtomatic RAdiometer) measures $\vec{T_B}$ and has been used in a series of field experiments carried out in the frame of the SMOS mission. More information on LAURA is provided in Section 4.1 and Villarino [2004].

2.3 Microwave radiometers

2.3.1 Real aperture radiometers

Real aperture radiometers scan across the field of view to measure the brightness temperature. Moreover, if they are flying at a height h the antenna size D required for a footprint d is $D = \lambda h/d$. For low-Earth orbit satellites operating at L-band, such as SMOS, an adequate ground resolution using real aperture radiometer implies an antenna size of several metres. This is impossible to implement for in-orbit sensors, but these radiometers are still being used in

ground-based experiments such as those described in this work. The configurations and main characteristics of real aperture radiometers are briefly described hereafter. Further information may be found in [Skou, 1989, Ulaby *et al.*, 1986].

Total power radiometer

The simplest radiometer schematic is that of a total power radiometer (TPR) shown in Fig. 2.4(a). The output

$$V_{\text{out}} = kBG(T_A + T_N) \tag{2.25}$$

is dependent on the radiometer gain G and noise temperature T_N. Gain variations are inherent to the performance of both gain and lossy microwave component, so TPR are not stable enough unless frequent calibrations are performed. On the contrary, the sensitivity of these radiometers

$$\Delta T = \frac{T_A + T_N}{\sqrt{B\tau_{\text{r}}}} \tag{2.26}$$

being τ_{r} the integration time, is the maximum than can be achieved if gain variations are neglected.

Dicke radiometer

The Dicke radiometer was proposed to solve the stability problems of total power radiometers. A Dicke radiometer views the scene during half the cycle and a matched load during the other half of the cycle. In this case, instead of the antenna temperature the difference between the antenna temperature and a known reference value T_R is measured:

$$V_{\text{out}} = c(T_A - T_R)G. \tag{2.27}$$

Note that this radiometer is more stable than TPR since the output does not depend on T_N and the weight of G can be diminished by choosing T_R values in the range of T_A. However, neglecting the gain fluctuations, the sensitivity of this configuration

$$\Delta T = 2\frac{T_A + T_R}{\sqrt{B\tau_{\text{r}}}}, \tag{2.28}$$

is degraded by a factor of 2 as compared to total power radiometers. The factor of two worse sensitivity arises from the fact that the scene is measured only half of the time.

Noise injection radiometer

Noise injection radiometers (NIR) are a modification of Dicke radiometers to obtain an output independent of G and T_N. As shown in Fig. 2.4(c) this configuration uses as input to the Dicke radiometer the signal $T'_A = T_A + T_I = (T_R - T_I) + T_I = T_R$, where T_I is a variable

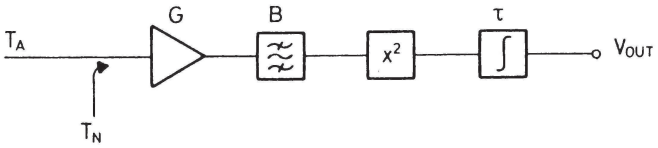

(a) Total power radiometer

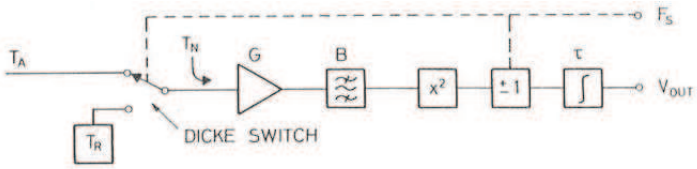

(b) Dicke radiometer

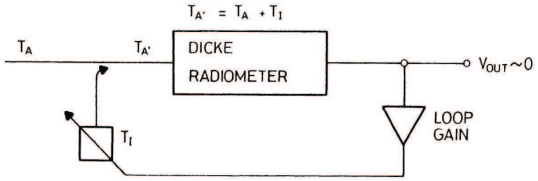

(c) Noise injection radiometer

Fig. 2.4: (a) Total power, (b) Dicke, and (c) noise injection radiometer schematic [Skou, 1989]

noise temperature. Since T'_A has the same value as T_R, then the radiometer output is zero:

$$V_{\text{out}} = c(T'_A - T_R)G = 0. \tag{2.29}$$

The sensitivity of noise injection radiometers is

$$\Delta T = 2\frac{T_R + T_N}{\sqrt{B\tau_{\text{r}}}}, \tag{2.30}$$

and it is independent of T_N and gain fluctuations.

2.3.2 Synthetic aperture radiometers

Synthetic aperture technology was proposed to solve the antenna size problem of real aperture radiometers commented on the previous section [LeVine & Good, 1983]. In this case, instead of a single big antenna many small antennæ are used. A two-dimensional image of the observed scenario is obtained by the cross-correlation of every pair of antennæ having an overlapping field of view. From this measurement, known as visibility, the brightness temperature image is obtained by inverse Fourier transformation. The first onboard two-dimensional synthetic aperture radiometer will be SMOS payload, MIRAS (see section 1.2.1). Further information may be found in Camps [1996].

Chapter 3

L-band emission of land covers

This chapter describes the properties of soils and vegetation, and revises the land emission models which are used at present in soil moisture retrieval algorithms from microwave remote sensing data.

3.1 Physical properties of soils

Soils consist of a mix of air, water, organic matter, and mineral particles. According to Jenny [1994], soils result from the combination of climate, organisms, relief, parent material, and time. This formulation is known as the CLORPT equation and determines the properties of each soil. Next sections briefly summarise the main soil physical properties. Further information on soil properties is reported, among others, in Brady & Weil [2003] and Behari [2005].

3.1.1 Texture

The size of mineral particles in soils usually ranges from below 0.002 mm to above 2 mm in diameter. The fraction above 2 mm is classed as gravel, and the fractions below 2 mm are classed as clay, silt, or sand as is indicated in Table 3.1. The relative proportions of clay, silt, and sand determines the soil texture. The three fundamental groups of soil are sands, loams, and clays, but there are many other types named according to the USDA soil classification triangle shown in Fig. 3.1.

Texture affects other soil properties as shown in Table 3.2. Fine-textured soils (clays) hold more water than coarse-textured soils (sands), and thus different soils will have a different dielectric constant behaviour (see Section 3.2) which will impact the intensity of the soil emission.

Table 3.1: Classification of soil particles as a function of their diameter (in mm)

Sand					Silt	Clay
very coarse	coarse	medium	fine	very fine		
2.0 to 1.0	1.0 to 0.5	0.5 to 0.25	0.25 to 0.10	0.10 to 0.05	0.05 to 0.002	<0.002

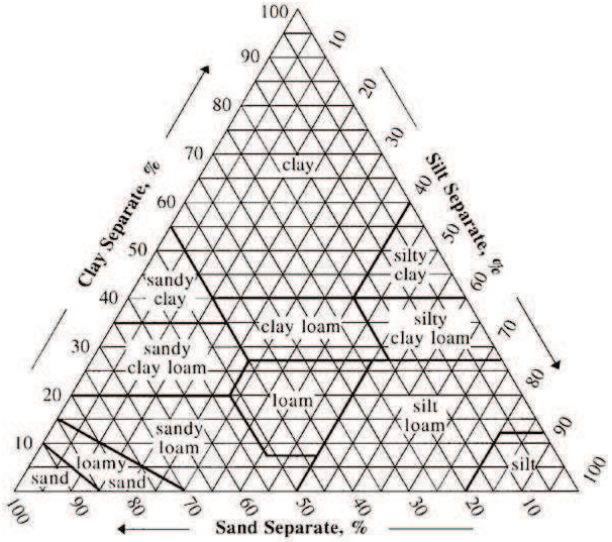

Fig. 3.1: USDA soil classification triangle

Table 3.2: Properties of soils as a function of texture

	Sand	Silt	Clay
Permeability	rapid	low to moderate	slow
Porosity	large pores	small pores	small pores
Water holding capacity	limited	medium	very large

3.1.2 Bulk and solid phase density

Soil bulk density ρ_b [g/cm^3] is defined as the ratio of the mass of dry solids to the bulk volume of the soil occupied by those dry solids:

$$\rho_b = \frac{\text{Mass of dry soil}}{\text{Volume of bulk soil}} = \rho_p \frac{c_\text{s} A_\text{s}}{D_\text{s} A_\text{s}} = \rho_p \frac{c_\text{s}}{D_\text{s}}, \tag{3.1}$$

being ρ_p the soil phase density, A_s the area, c_s the equivalent depth filled with solid, and D_s the total equivalent density of the soil made up of solids, water, and air. The density of the solid phase is constant for a soil type, and varies from 1.3 to 2.1 g/cm^3 in sands, from 1.2 to 2.6 g/cm^3 in clays, and from 0.8 to 1.6 g/cm^3 in loams [Chukhlantsev, 2006, p. 21–23]. On the contrary, the bulk density has not a unique value since depends on compaction, swelling, etc. Porous soils have low ρ_b and those compact have higher values. The range of possible values varies from 1 to 1.6 g/cm^3 for clay, clay loam, and silt loam soils, and from 1.2 to 1.8 g/cm^3 in sands and sandy loams.

3.1.3 Pore space or porosity

Pores are the void spaces between soil particles. Pore spaces of dry soils are mostly filled with air, while water fills the pores of wet soils. Processes such as infiltration, ground-water movement, and storage occur in these void spaces. Porosity is in turn affected by texture, soil

structure, compaction, and organic matter. The porosity is determined from the bulk density ρ_b and particle density ρ_p (see Section 3.1.2) as

$$P_{\mathrm{s}} = 1 - \frac{\rho_b}{\rho_p}. \tag{3.2}$$

Pores in a soil have a large variability in arrangement, size, and shape. Sands have very few small pores which hold water, while clays have many large pores which are needed for the rapid water intake and distribution of water. Typical values of the porosity range from 25–50% in sands, from 35–50% in loams, and from 33–60% in clays [Fetter, 2001].

3.1.4 Permeability and water holding capacity

Permeability is the rate at which fluid can flow through the soil pores, while water-holding capacity is the ability of soils to hold water for plant use. Both parameters are a function of soil structure, porosity, and texture as summarised in Table 3.2.

3.1.5 Structure

Soil structure refers to the way sand, silt, and clay particles are arranged into clumps or aggregates. The aggregates are bound together by clay and organic matter. Structure affects drainage, root growth, infiltration, germination, and aeration.

3.1.6 Temperature

Soil temperature determines the chemical reaction within a soil and, thus, plants growth, water movement and availability of nutrients. Soil temperature depends on meteorological and physical soil properties such as colour, surface roughness, and water content. For instance, dark soils absorb more heat than smooth light-coloured ones and thus warm faster. On its part, soil moisture affects the rate of temperature change: more heat is needed to warm a wet soil than a dry one. The temperature of soils follows the temperature of the air, but with a time lag. This effect diminishes with soil depth.

3.1.7 Water in soils

Although there is not a unique classification of water in soils, the common classification divides it into bound and free water. Bound water is the water adsorbed by the surface of soil particles, while free water is the liquid water located in the pore spaces. Bound water depends on soil texture and takes the minimum values (2–3%) in sands, and the maximum (20–40%) in clays. The soil moisture, or water in a soil, is usually determined in two ways:

- Gravimetric soil moisture w_g, which depends on the wet and dry weights of the soil sample (w_w and w_d respectively),

$$w_g = \frac{w_w - w_d}{w_d}, \tag{3.3}$$

- Volumetric soil moisture m_v, which depends on the volume of water V_w, the volume of the soil sample V_s, the soil bulk density ρ_b, and the density of wet soil ρ_{ws} and water ρ_w,

$$w_s = \frac{V_w}{V_s} = w_g \frac{\rho_{ws}}{\rho_w} = m \frac{\rho_b}{\rho_w}. \tag{3.4}$$

The field capacity and wilting pointing are, among other hydrological parameters, involved in the dielectric constant models. The field capacity (FC) is the amount of water held in a soil after excess water has drained away. Physically, it is the water held at a soil at a tension of 1/3 bar. The field capacity can be estimated from the volumetric soil moisture and the weight fractions (in %) of sand S and clay C as [Wang & Schmugge, 1980]

$$\mathrm{FC} = 0.3 - 0.25S + 0.5C. \tag{3.5}$$

The wilting point (WP) is the level of soil moisture below which plants wilt, and is usually taken as the soil moisture at a tension of 15 bar. The wilting point is estimated from the textural composition as [Wang & Schmugge, 1980],

$$\mathrm{WP} = 0.06774 - 0.00064S + 0.00478C. \tag{3.6}$$

The difference between field capacity and wilting point is the available water content.

3.2 Dielectric constant of soils

The dielectric constant determines the response of the soil to an incident electromagnetic wave. This response is composed of two parts (real and imaginary), which determine the wave velocity and energy losses respectively. In a non-homogeneous medium such as soils, the dielectric properties have a strong impact on its microwave emission. However, the relationship between the soil dielectric constant ($\varepsilon_s = \varepsilon'_s + j\varepsilon''_s$), and the soil physical properties is not straightforward. A large number of studies have been performed during the last decades to find out this relationship since it plays an important part in the soil moisture retrieval algorithms from remote sensing data [Birchak *et al.*, 1974, Hipp, 1974, Wang & Schmugge, 1980, Topp *et al.*, 1980, Hallikainen *et al.*, 1985, Dobson *et al.*, 1985, Shutko & Reutov, 1982, Mironov *et al.*, 2004, Roth *et al.*, 1992, Miller & Gaskin, 1999, Peplinsky *et al.*, 1995, Curtis, 2001, Calvet *et al.*, 1995]. Some of these models are simple empirical models in which data is fitted by a curve unique for all soils; others propose semi-empirical approaches which take into account some soil physical properties.

The dielectric constant of dry soils is almost independent of temperature [Topp *et al.*, 1980] and frequency. On the contrary, wet soils show a complex behaviour depending on the interaction between soil, water, and air particles. Hallikainen *et al.* [1985] performed a series of dielectric constant measurements of five soils with different texture composition at frequencies between 1.4 and 18 GHz and found out that texture has a strong effect on the dielectric behaviour which is specially pronounced at frequencies below 5 GHz. Results at 1.4 GHz, which is our frequency of

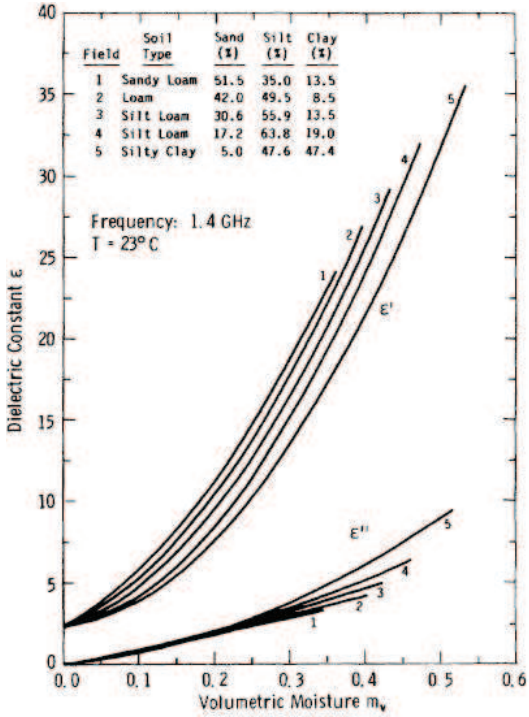

Fig. 3.2: Measured dielectric constant at 1.4 GHz for five soils with different textural composition, from Hallikainen *et al.* [1985, Fig. 6(a)]

interest, are shown in Fig. 3.2. In the dielectric-mixing model by Roth *et al.* [1992], differences in soil texture and bound water and free water are ignored altogether.

Next sections review some of the most commonly used dielectric constant models. For further information refer to Behari [2005] and Chukhlantsev [2006].

3.2.1 Empirical approach

Empirical approaches fit curves to measured data without taking into account the soil physics. This is, for instance, the approach followed by in Topp *et al.* [1980], where the dielectric constant of mineral soils ε is related to the volumetric moisture content measured using TDR techniques w_s by a third order polynomial:

$$w_s = 4.3 \cdot 10^{-6}\varepsilon_s^3 - 5.5 \cdot 10^{-4}\varepsilon_s^2 + 2.92 \cdot 10^{-2}\varepsilon_s - 5.3 \cdot 10^{-2}. \tag{3.7}$$

This equation has been successfully used by many authors over different soils and even ice, although others have found out that soil moisture content was under- or overestimated. Noborio [2001] offers a complete reference of these studies.

3.2.2 Semi-empirical approach

Other models use a semi-empirical approach that contains a model of the complex dielectric constant and the volume fraction of each of the soil components. This kind of approach was used by Wang & Schmugge [1980], Dobson *et al.* [1985] and Roth *et al.* [1992]. In most cases,

the starting point is the dielectric mixing model by Birchak *et al.* [1974]:

$$\varepsilon_s^\alpha = V_{\rm sp}\varepsilon_{\rm sp}^\alpha + V_{\rm a}\varepsilon_{\rm a}^\alpha + V_{\rm fw}\varepsilon_{\rm fw}^\alpha + V_{\rm bw}\varepsilon_{\rm bw}^\alpha, \tag{3.8}$$

where $V_{\rm sp}$ ($\varepsilon_{\rm sp}$), $V_{\rm a}$ ($\varepsilon_{\rm a}$), $V_{\rm fw}$ ($\varepsilon_{\rm fw}$) and $V_{\rm bw}$ ($\varepsilon_{\rm bw}$) are the volume fraction (dielectric constant) of solid phase, air, free water, and bound water in the soil, respectively. The expression in (3.8) can be rewritten as a function of the bulk density and the volumetric moisture as

$$\varepsilon_s^\alpha = 1 + \frac{\rho_b}{\rho_s}(\varepsilon_{\rm sp}^\alpha - 1) + V_{\rm fw}\varepsilon_{\rm fw}^\alpha + V_{\rm bw}\varepsilon_{\rm bw}^\alpha - w_s. \tag{3.9}$$

If $\alpha = 0.5$ the model in (3.9) is known as refractive model.

Wang and Schmugge model

The Wang & Schmugge [1980] model was proposed for 1.4 and 5 GHz frequencies and starts from (3.9) with $\alpha = 1$. This model provides separate dielectric constant equations for volumetric water content lower than, or greater than the transition moisture w_t. The transition moisture is the moisture content at which the free water phase begins to dominate the soil hydraulics, and is strongly dependent on texture. It is determined from the wilting point (see Section 3.1.7) as

$$w_t = 0.49{\rm WP} + 0.165. \tag{3.10}$$

The soil dielectric constant is then estimated as:

$$\varepsilon_s = \begin{cases} w_s\varepsilon_{\rm x} + (P_{\rm s} - w_s)\varepsilon_{\rm a} + (1 - P_{\rm s})\varepsilon_{\rm r} & w_s < w_t, \\ w_t\varepsilon_{\rm x} + (w_s - w_t)\varepsilon_{fw} + (P_{\rm s} - w_s)\varepsilon_{\rm a} + (1 - P_{\rm s})\varepsilon_{\rm r} & w_s > w_t, \end{cases} \tag{3.11}$$

with

$$\varepsilon_{\rm x} = \begin{cases} \varepsilon_{\rm i} + (\varepsilon_{fw} - \varepsilon_{\rm i})\frac{w_s}{w_t}\gamma & w_s < w_t, \\ \varepsilon_{\rm x} = \varepsilon_{\rm i} + (\varepsilon_{fw} - \varepsilon_{\rm i})\gamma & w_s > w_t, \end{cases} \tag{3.12}$$

and

$$\gamma = -0.57w_t + 0.481, \tag{3.13}$$

being $\varepsilon_{\rm i}$, $\varepsilon_{\rm a}$, ε_{fw}, and $\varepsilon_{\rm r}$ the dielectric constants of ice, air, free water, and rock, respectively, and $\varepsilon_{\rm x}$ is the dielectric constant of the initially adsorbed water.

Dobson et al. model

The Dobson *et al.* [1985] model starts from (3.9) and makes the following assumption

$$V_{\rm fw}\varepsilon_{\rm fw}^\alpha + V_{\rm bw}\varepsilon_{\rm bw}^\alpha = w_s^\beta\varepsilon_{\rm fw}^\alpha, \tag{3.14}$$

which means that there is not distinction between bound and free water. Taking this into account, the new expression for the dielectric constant is

$$\varepsilon_s = \left(1 + \frac{\rho_b}{\rho_s}(\varepsilon_{\rm sp}^{\alpha} - 1) + w_s^{\beta}\varepsilon_{\rm fw}^{\alpha} - w_s\right)^{\frac{1}{\alpha}}. \tag{3.15}$$

The real and imaginary parts of the dielectric constant of soils are obtained separately as [Dobson *et al.*, 1985, Peplinsky *et al.*, 1995]

$$\begin{aligned} \varepsilon_s' &= \left(1 + \frac{\rho_b}{\rho_s}(\varepsilon_{\rm sp}^{\alpha} - 1) + w_s^{\beta'}\varepsilon_{\rm fw}'^{\alpha} - w_s\right)^{\frac{1}{\alpha}}, \\ +\varepsilon_s''^{\alpha} &= w_s^{\beta''}\varepsilon_{\rm fw}''^{\alpha}, \end{aligned} \tag{3.16}$$

where β' and β'' are obtained from the percentage of clay C and sand S in the soil,

$$\beta' = (127.48 - 0.519S - 0.152C)/100, \tag{3.17}$$

$$\beta'' = (1.33979 - 0.603S - 0.166C)/100, \tag{3.18}$$

and $\varepsilon_{\rm fw}$ is the dielectric constant of free water, which is estimated using the Debye equation:

$$\varepsilon_{\rm fw} = \varepsilon_{\rm w\infty} + \frac{\varepsilon_{\rm w0} - \varepsilon_{\rm w\infty}}{1 + j2\pi f\tau_{\rm w}} - j\frac{\sigma_{\rm eff}}{2\pi f\varepsilon_0}\frac{\rho_s - \rho_b}{\rho_s w_s}, \tag{3.19}$$

being $\varepsilon_{\rm w\infty} \approx 4.9$ the high frequency limit of ε_{fw}, $\varepsilon_{\rm w0}$ the static dielectric constant of water, $\varepsilon_0 = 8.854 \cdot 10^{-12}$ F/m the permittivity of free space, f the frequency in Hz, $\tau_{\rm w}$ the relaxation time of water, and

$$\sigma_{\rm eff} = -1.645 + 1.939\rho_b - 0.02013S + 0.01594C. \tag{3.20}$$

3.3 Emission from land covers

Microwave remote sensing is based on the measurement of the thermal radiation or brightness temperature of a target, which is determined by its physical temperature and emissivity (see Chapter 2). The emissivity of land covers depends on soil moisture, but also on soil temperature [Choudhury *et al.*, 1982, Wigneron *et al.*, 2001, Holmes *et al.*, 2006], soil surface roughness [Mo & Schmugge, 1987, Wigneron *et al.*, 2001, Escorihuela *et al.*, 2007], vegetation canopy [Brunfeldt & Ulaby, 1984, Jackson & Schmugge, 1991, Ferrazzoli *et al.*, 2002, Della Vecchia *et al.*, 2006], snow cover [Schwank *et al.*, 2004], relief [Mätlzler & Standley, 2000, Talone *et al.*, 2007], etc.

During this PhD Thesis a series of field experiments were performed to determine the impact of some of the fore-mentioned parameters in the measured emission of land (see Chapter 4). The fundamentals of microwave emission from land covers are presented hereafter.

3.3.1 Bare soils

The emissivity of bare soils is given by

$$e_s = 1 - \Gamma_s \tag{3.21}$$

where Γ_s is the total reflectivity. The total reflectivity at p polarisation ($p = h, v$) in a chosen observation direction is expressed in terms of the bistatic scattering coefficients (σ_{pp}, σ_{pq}) as follows [Fung, 1994]:

$$\Gamma_{s,p}(\theta_i, \phi_i) = \frac{1}{4\pi} \int_{4\pi} [\sigma_{pp}(\theta_i, \phi_i, \theta_r, \phi_r) + \sigma_{pq}(\theta_i, \phi_i, \theta_r, \phi_r)] d\Omega_r. \tag{3.22}$$

Subscripts i and r stand for the incident and scattered radiation, and θ and ϕ are the incidence and azimuth angles, respectively. The coefficient σ_{pp}, often called co-polar component, considers the scattering on the observation direction and polarisation, while σ_{pq}, or cross-polar component, considers the scattering in whatever other direction and polarisation. The integration over the entire half space and errors in the modelling of the bistatic scattering coefficients make the computation of (3.22) unfeasible or prone to errors. For this reason, the uniform half space model with smooth surface is commonly adopted. This model is simpler and thus suitable to be used in soil moisture retrieval algorithms from remotely sensed data. In this case, the total reflectivity in (3.22) equals the reflection coefficient given by the Fresnel formulation

$$\begin{aligned} \Gamma_{oh} &= \left| \frac{\cos\theta - \sqrt{\varepsilon_s - \sin^2\theta}}{\cos\theta + \sqrt{\varepsilon_s - \sin^2\theta}} \right|^2, \\ \Gamma_{ov} &= \left| \frac{\varepsilon_s \cos\theta - \sqrt{\varepsilon_s - \sin^2\theta}}{\varepsilon_s \cos\theta + \sqrt{\varepsilon_s - \sin^2\theta}} \right|^2, \end{aligned} \tag{3.23}$$

where ε_s is the dielectric constant of soils, which is estimated using a model such as those summarised in Section 3.2.

3.3.2 Soil surface roughness

The effect of soil surface roughness on the brightness temperature has been an issue widely addressed in the literature [Choudhury *et al.*, 1979, Wang & Choudhury, 1981, Mo & Schmugge, 1987, Wang, 1983, Schneeberger *et al.*, 2004, Escorihuela *et al.*, 2007, Wegmüller & Mätzler, 1999, Wigneron *et al.*, 2001]. Fung [1994] proposes a theoretical physical model based on surface characteristics derived from the measured soil height profile. A simple empirical roughness model which takes into account only the coherent term of the scattering was reported in Choudhury *et al.* [1979]

$$\Gamma_{sp} = \Gamma_{op} \exp(-4k_\lambda^2 \sigma_s^2 \cos^2(\theta)), \tag{3.24}$$

where Γ_{op} is the reflectivity of a smooth surface given by (3.23), $k = 2\pi/\lambda$ is the electromag-

netic wave number, σ_s is the standard deviation of the surface height, and θ is the incidence angle. This model was reviewed, and another formulation was proposed in Wang & Choudhury [1981]:

$$\Gamma_p(\theta) = [(1 - Q_s)\Gamma_{op}(\theta) + Q_s\Gamma_{oq}(\theta)] \exp(-h_s \cos^n \theta). \tag{3.25}$$

In this case, two semi-empirical parameters were included to model the effects of the polarisation mixing (Q_s), and surface roughness (h_s and n). The dependence of these parameters on surface properties such as correlation length (l_c) or standard deviation of height (σ_s) is not yet clear. Mo & Schmugge [1987] and Wigneron *et al.* [2001] conclude that the $n = 2$ dependence proposed in Choudhury *et al.* [1979] is too strong for L-band. A value of $n = 0$ at both polarisations was found to be consistent with measurements in Wigneron *et al.* [2001], while Escorihuela *et al.* [2007] distinguishes n values for both polarisations (1 at horizontal and -1 at vertical). Similarly, there are discrepancies on the value of the roughness parameter h_s. Some authors obtain h_s from experimental data by best-fit [Wigneron *et al.*, 2001] while others propose expressions for h_s as a function of geophysical parameters. Mo & Schmugge [1987] obtain good results with two parameterisations of h_s as a function of σ_s and l_c. Finally, there is a general agreement on the value of the cross-polarisation parameter Q_s, which has been found to be very small (0 to 0.12) at L-band [Mo & Schmugge, 1987, Wigneron *et al.*, 2001].

Apart from these considerations, the effects of frequency and incidence angle on the roughness parameters have not been studied thoroughly. Mo & Schmugge [1987] and Shi *et al.* [2002] pointed out that the roughness effects depend on both of the frequency and the incidence angle. Shi *et al.* [2002] suggested a parametrisation of the surface reflectivity derived from data simulated for a wide range of soil water content and roughness properties using the integral equation model [Fung, 1994]. The surface reflectivity model of Shi *et al.* [2002] was tested in Schneeberger *et al.* [2004] and found not to be capable of explaining discrepancies between the ground truth and remotely sensed data. As a consequence, a new model was developed for describing the influence of the topsoil structure on the L-band emission as an impedance matching between the dielectric constants of soil and air [Mätzler, 2006, Section 4.7].

3.3.3 Vegetation

If the remote sensor is placed above a canopy looking downwards, the measured brightness temperature will contain not only information on the soil, but also on vegetation, since vegetation radiates its own energy and, moreover, attenuates and scatters the soil radiation. Chukhlantsev [2006] revised the theory and conducted experimental research over vegetated areas. Although the modelling of the land emission involves analytical solutions of the radiative transfer equation [Ferrazzoli *et al.*, 2002, Della Vecchia *et al.*, 2006, Ferrazzoli & Guerriero, 1996], this approach is not easy to use with experimental data. Hence, the common practice is to use approximate formulas or semi-empirical models in which the different components of the brightness temperature could be differentiated. The emissivity of a soil covered by vegetation is usually estimated as the contribution of three terms: (i) the radiation from the soil that is attenuated by the overlying

vegetation, (ii) the upward radiation from the vegetation, and (iii) the downward radiation from the vegetation, reflected by the soil, and attenuated by the canopy [Ulaby *et al.*, 1986, p. 888]:

$$T_{Bp}^{\text{model}} = \left(1 + \frac{1 - e_{\text{bs}}}{L_{\text{veg}}}\right)\left(1 - \frac{1}{L_{\text{veg}}}\right)(1 - \omega)T_{\text{veg}} + \frac{e_{\text{bs}}}{L_{\text{veg}}}T_{\text{s}}, \tag{3.26}$$

where e_{bs} is the emissivity of a bare soil, T_{veg} and T_{soil} are the physical temperatures of the vegetation and soil, respectively, $L_{\text{veg}} = \exp(\tau \cdot \sec\theta)$ is the attenuation due to the vegetation cover, $\tau = b{\cdot}\text{VWC}$ is the optical thickness, b is the b-factor [Van de Griend & Wigneron, 2004], VWC is the vegetation water content, and ω is the single scattering albedo. This formulation is known as the $\tau-\omega$ model Van de Griend & Wigneron [2004] and is based on the single scattering approach proposed in Kirdiashev *et al.* [1979]. The optical depth is related to the vegetation density and the frequency. The single scattering albedo describes the scattering of the emitted radiation by the vegetation, and is a function of plant geometry.

3.3.4 Soil effective temperature

Soil microwave brightness temperature depends on soil emission and on the soil effective temperature, T_{eff}. The theoretical effective temperature of a soil profile can be estimated as [Ulaby *et al.*, 1986]:

$$T_{\text{eff}} = \int_0^\infty T(z)\alpha(z)\exp\left[-\int_0^x \alpha(z')dz'\right]dz, \tag{3.27}$$

where T is the thermodynamic temperature, and α is the attenuation coefficient at a depth z. The attenuation is a function of the soil dielectric constant, $\varepsilon_s = \varepsilon_s' + j\varepsilon_s''$, and of the microwave emission wavelength λ:

$$\alpha(z) = \frac{4\pi}{\lambda}\frac{\varepsilon_s''(z)}{2\sqrt{\varepsilon_s'}(z)}. \tag{3.28}$$

Several simple formulations have been developed to estimate the soil effective temperature from soil properties, and soil moisture and temperature profiles. Choudhury *et al.* [1982] proposed a parametrisation of T_{eff} based on the soil temperature at deep soil (T_∞) corresponding to a depth between 50 cm and 1 m, and on a "surface" temperature (T_{surf}) corresponding to a depth of 0–5 cm:

$$T_{\text{eff}} = T_\infty + C_s(T_{\text{surf}} - T_\infty). \tag{3.29}$$

The coefficient C_s was considered constant for a given frequency, and equal to 0.246 at L-band.

On the other hand, Chanzy *et al.* [1997] presented a model for the soil effective temperature at L- and C-bands based on the air temperature, a deep soil temperature, and the brightness temperature measured at X-band and V-pol.

Wigneron *et al.* [2001] proposed a parametrisation based on (3.29), but with a coefficient C_s dependent on the volumetric water content w_s, and two semi-empirical parameters (w_0 and

b_{w_0}):

$$T_{\text{eff}} = T_\infty + (T_{\text{surf}} - T_\infty)\left(\frac{w_s}{w_0}\right)^{b_{w_0}}. \tag{3.30}$$

Another formulation using the soil dielectric constant instead of the volumetric water content was proposed by Holmes *et al.* [2006]. The performance of (3.29) and (3.30) if soil properties such as texture and density were accounted for in the determination of the C_s parameter is analysed in Wigneron *et al.* [2008].

3.4 Soil moisture retrieval algorithms

This PhD Thesis focuses on empirical soil emission modelling and moisture retrieval within the SMOS mission. The basics of microwave remote sensing have been discussed in Chapter 2 and in the previous Sections of this Chapter, and constitute the basis for the soil moisture retrieval algorithms. The brightness temperature of land covers is influenced by many variables, the most important being soil moisture and temperature, and vegetation characteristics. The challenge is to reconstruct the environmental parameters from the measured signal by using a minimum of ancillary data. To do this, different soil moisture retrieval algorithms have been developed. Some of them were summarised in the review by Wigneron *et al.* [2003].

The first one is based on the experimental relationship between the geophysical variables and the radiative transfer equation using a regression technique. This approach has limited applicability, since often the regression is valid only for the test sites where they were obtained.

The second approach is based on the use of neural networks. These algorithms have been used with satisfactory results in the retrieval of agricultural parameters from radiometric data [Del Frate *et al.*, 2003, Del Frate & Wang, 2001], but need a training phase that is not always feasible.

The third type of algorithms is widely used and is based on the inversion of radiative transfer models. Obviously, this approach has also disadvantages, since errors of the model lead to errors in the retrieval. The soil moisture models are used as forward models, and the geophysical variables are retrieved by minimisation of a cost function of the type [Parde *et al.*, 2004, Saleh *et al.*, 2006a]:

$$F = \sum_\theta \frac{(T_{Bh} - T_{Bh}^{\text{meas}})^2 + (T_{Bv} - T_{Bv}^{\text{meas}})^2}{\sigma_{T_B^2}} + \sum_n \frac{(P_n^{\text{ini}} - P_n)^2}{\sigma_{P_n}^2}. \tag{3.31}$$

where the simulated brightness temperature T_{Bp} is computed using a land emission model as those in Section 3.3, T_{Bp}^{meas} is the measured brightness temperature, and P_n is any of the parameters on which T_{Bp} depends. A first-guess value of the parameter P_n (P_n^{ini}) with associated standard deviation σ_{Pn} can be also considered in the cost function. Estimates can be constrained to be close to the initial value by choosing low σ_{Pn} values, or they can be left as a free parameter by selecting $\sigma_{Pn} \gg 1$.